spacecraft on 31 March 2002 starting at 15:58:14.245 at a distance of $8.85R_e$ (with R_e the radius of Earth) and at 11.18 magnetic local time (MLT) (Fig. 4B). The localized bipolar parallel electric field is consistent with previously published satellite data (*18*–*21*). To model the parallel electric field that might be seen by a satellite crossing the magnetopause as a result of the rapid convection of electron holes, we plot E_z obtained along a trajectory in the *x*-*z* plane through the hole in our simulation (Fig. 2B) at an angle of 10° with respect to the *z* axis. The strongly localized bipolar parallel electric field is consistent with the Polar data. Note, however, that the parity of the holes in the data is inverted compared with the simulation. The parity depends on the direction of the electron hole velocity compared with the direction of the ambient magnetic field. Both parities are seen in the spacecraft data.

The comparison with satellite data is complicated by the fact that the simulations cannot at the present time be carried out with realistic electron to ion mass ratios. Also, the simulations presented have $\omega_{pe} < \Omega_{ce}$ while at the magnetopause the inequality is reversed. The simulations therefore have to be extrapolated to the magnetopause using the theoretical scaling of the size of the electron hole, $L_h \sim 2\pi v_{de}/\omega_{pe}$, its velocity $v_h \sim (m_e/m_i)^{1/3} v_{de}$, and the maximum potential ϕ_h, given by the smaller of the expressions in Eqs. 6 and 7. The primary uncertainty in comparing with the satellite data concerns the electron streaming velocity. The sweep time to measure the electron velocity distribution on Polar is around 4 s, whereas trains of electron holes typically last 0.1 s or less and single holes transit in 10^{-3} s. The combination of the wave train duration and the typical relative drift speed of 10 km/s between the magnetopause and spacecraft implies that electron holes are localized to regions of transverse (to the magnetopause) scale around 1 km, which is roughly the electron skin depth c/ω_{pe} and is consistent with the simulations. Because such narrow electron beams are not measurable with Polar, it is not possible to correlate beam parameters with electron hole velocities. In the absence of adequate data on the electron drift speed, we can check the self-consistency of the measured hole velocity and scale length by eliminating the electron drift speed, which yields the relation $L_h \sim 2\pi(v_h/\omega_{pe})(m_i/m_e)^{1/3}$. The plasma density during the time interval in Fig. 4B is around $4/cm^3$ (based on the measurement of the spacecraft potential) and the measured hole velocity is 260 km/s. The predicted hole scale length is therefore around 0.7 km compared with the measured value of 1.4 km. This relationship has also been tested on the basis of five magnetopause crossings where high–time resolution electric field and electron density moment data from Polar are available. The hole velocities in this data set have a range $v_h \sim 250$ to 2000 km/s. The predicted hole size scaling agrees well with Polar data (Fig. 4D). The measured hole potentials in this same data set range from 0.1 to 10 V. Comparison with theory is again complicated by the absence of resolved data on the electron streaming velocity. Taking $v_{de} \sim (m_i/m_e)^{1/3} v_h \sim 3200$ km/s for the observed hole (Fig. 4B), we estimate $e\phi \sim m_e v_{de}^2/2 \sim 30$ eV, compared with $e\phi \sim 10$ eV from the Polar data. On the other hand, for $T_e \sim 50$ eV, $v_{te} \sim 2800$ km/s, hence a drift speed of 3200 km/s is close to marginal stability of the Buneman instability.

Consistent with the 3D simulations, strong lower hybrid waves are typically measured in satellite crossings of the magnetopause where bursts of electron holes are observed. In satellite observations of electron holes in the auroral ionosphere, waves in the lower hybrid range of frequencies are also observed (*23*). However, the coupling of these distinct classes of wave fields in the satellite data has not yet been explored. The inverse problem, driving electron parallel current with lower hybrid waves, has been explored for many years in laboratory fusion experiments (*24*). Thus, the role of such waves as a mechanism for retarding current should not be surprising.

References and Notes

1. E. N. Parker, *J. Geophys. Res.* **62**, 509 (1957).
2. P. A. Sweet, in *Electromagnetic Phenomena in Cosmical Physics*, B. Lehnert, Ed. (Cambridge Univ. Press, New York, 1958), p. 123.
3. D. Biskamp, *Phys. Fluids* **29**, 1520 (1986).
4. A. A. Galeev, R. Z. Sagdeev, *Handbook of Plasma Physics* (North-Holland Physics, Amsterdam, 1984), vol. 2, chap. 6.1, p. 271.
5. H. E. Petschek, in *AAS/NASA Symposium on the Physics of Solar Flares*, W. N. Ness, Ed. (NASA, Washington, DC, 1964), p. 425.
6. T. Sato, T. Hayashi, *Phys. Fluids* **22**, 1189 (1979).
7. R. P. Lin, H. S. Hudson, *Sol. Phys.* **17**, 412 (1971).
8. M. Oieroset, R. P. Lin, T. D. Phan, D. E. Larson, S. D. Bale, *Phys. Rev. Lett.* **89**, 195001 (2002).
9. M. Temerin, K. Cerny, W. Lotko, F. S. Mozer, *Phys. Rev. Lett.* **48**, 1175 (1982).
10. F. Mozer, R. Ergun, M. Temerin, C. Cattell, *Phys. Rev. Lett.* **79**, 1281 (1997).
11. A. Zeiler *et al.*, *J. Geophys. Res.* **107**, 1230 (2002).
12. O. Buneman, *Phys. Rev.* **115**, 503 (1959).
13. S. Bujarbarua, H. Schamel, *J. Plasma Phys.* **25**, 515 (1981).
14. Y. Omura, H. Matsumoto, T. Miyake, H. Kojima, *J. Geophys. Res.* **101**, 2685 (1996).
15. D. L. Newman, M. V. Goldman, R. E. Ergun, A. Mangeney, *Phys. Rev. Lett.* **87**, 255001 (2001).
16. N. Shimada, M. Hoshino, *Astrophys. J.* **543**, L67 (2000).
17. A. B. Mikhailovskii, *Theory of Plasma Instabilities, Vol. 1* (Consultants Bureau, New York, 1974).
18. J. Franz, P. Kintner, J. Pickett, *Geophys. Res. Lett.* **25**, 1277 (1998).
19. H. Matsumoto, L. A. Frank, Y. Omura, H. Kojima, *Geophys. Res. Lett.* **26**, 421 (1999).
20. C. Cattell, J. Dombeck, J. R. Wygant, M. K. Hudson, *Geophys. Res. Lett.* **26**, 425 (1999).
21. C. Cattell, J. Crumley, J. Dombeck, J. Wygant, F. S. Moser, *Geophys. Res. Lett.* **29** (no. 5), 9-1 (2002).
22. M. Swisdak, B. N. Rogers, J. F. Drake, M. A. Shay, *J. Geophys. Res.*, in press.
23. R. Pottelette, R. Treumann, M. Berthomier, *J. Geophys. Res.* **106**, 8465 (2001).
24. M. Porkolab, R. P. H. Chang, *Rev. Mod. Phys.* **50**, 745 (1978).

25. Supported in part by the U.S. Department of Energy, NASA, and NSF. We thank M. Porkolab for helpful discussions on the structure on the lower hybrid wave.

Supporting Online Material

www.sciencemag.org/cgi/content/full/299/5608/873/DC1

Movies S1 and S2

11 November 2002; accepted 13 December 2002

Eocene El Niño: Evidence for Robust Tropical Dynamics in the "Hothouse"

Matthew Huber*† and Rodrigo Caballero

Much uncertainty surrounds the interactions between the El Niño–Southern Oscillation (ENSO) and long-term global change. Past periods of extreme global warmth, exemplified by the Eocene (55 to 35 million years ago), provide a good testing ground for theories for this interaction. Here, we compare Eocene coupled climate model simulations with annually resolved variability records preserved in lake sediments. The simulations show Pacific deep-ocean and high-latitude surface warming of ~10°C but little change in the tropical thermocline structure, atmosphere-ocean dynamics, and ENSO, in agreement with proxies. This result contrasts with theories linking past and future "hothouse" climates with a shift toward a permanent El Niño–like state.

Whereas ENSO's interannual impact on the global climate and the carbon cycle is well established (*1*–*3*), the role of the tropical Pacific in long–time-scale climate change remains controversial (*4*, *5*). The Pacific ocean-atmosphere system is governed by a delicate balance of dynamical feedbacks (*6*–*8*), raising concern about its stability to external forcing. Conceivably, the region's climate could undergo major, long-term reorganizations (*9*), which could strongly modulate global change. In particular, theory indicates that any changes acting to weaken the "Bjerknes" feedback—the instability at the

heart of the tropical Pacific climate (*10*)—might lead to reduced ENSO variability and eventually to its complete shutdown (*7*, *11*, *12*). In these circumstances, the system collapses onto a permanent El Niño–like state with a weak thermocline tilt, little or no upwelling in the east, and a small sea surface temperature (SST) gradient along the equator. The climate impacts observed during a modern El Niño event, including higher global mean temperatures (*1*), increased heat export to the extratropics (*13*), and continental warmth over parts of North America (*4*), would presumably become a permanent fixture of global climate (*4*, *14*). A permanent El Niño could explain features of past climates such as high-latitude warmth and provide a possible amplifying mechanism for future global warming. Assessing the robustness of the tropical Pacific climate is thus a key issue for understanding both past and future climate change. Such an assessment within the context of past, warm climates offers the advantage that model predictions can be directly compared with available proxy data. We argue that the Eocene provides a particularly exacting test of the robustness of ENSO and the mean east-west thermocline tilt.

The Eocene climate was much warmer than that of today. Geological proxies indicate extreme polar amplification of the warming, with extratropical continental temperatures above freezing year-round and deep-ocean temperatures ~10°C higher than at present (*15*). Tropical temperatures increased substantially less (*16*). One of the proposed routes leading to a permanent El Niño involves precisely this polar amplification, which, through the mediation of the thermohaline circulation, entails a reduction of the temperature difference between the ocean surface and the deep ocean. Assuming that this leads to a deepening of the equatorial thermocline and/or a reduction of the temperature difference across it, the result is a weakened Bjerknes feedback leading to ENSO suppression (*17*). Some studies indicate an ENSO shutdown as recently as ~6000 years ago (*18*), a period only slightly warmer than the present. This result, if explained by the above mechanism, suggests that the tropics are currently perched on the edge of the "collapsed" state (*17*). Other data, however, indicate only a reduction in ENSO amplitude (*19*), possibly accounted for by other processes (*20*).

A range of greenhouse gas (GHG) concentrations have been proposed for the Eocene, most of them significantly higher than modern (*21*). Studies of future transient global warming with coupled ocean-atmosphere models (*22, 23*) find a shift to a more El Niño–like state through local radiative processes amplified by the large-scale circulation. Although these models now fairly accurately simulate both present-day ENSO and the mean tropical climate without recourse to flux "corrections" (*24, 25*), model responses to GHG forcing still strongly depend on details of the sub–grid-scale parameterizations, especially cloud treatments, and the "permanent El Niño state" is by no means uniformly predicted by a majority of models (*23, 24*).

In the Eocene, the Panamanian and Indonesian seaways were unobstructed, which, it has been argued, should lead to a deepening of the thermocline in the eastern Pacific (*26*) or a shoaling in the west (*14*, *27*), respectively. In either case, the result is a reduction of the mean thermocline tilt and, again, a weaker Bjerknes feedback. The approximate coincidence of the closing of the Panamanian and Indonesian seaways with the onset of the Northern Hemisphere Ice Age ~3 million years ago has led some authors to suggest that a permanent El Niño prevailed during the pre–Ice Age Pliocene (*14*), generating high-latitude warmth.

Thus, all proposed mechanisms leading to a weakening of the Bjerknes feedback and a shutdown of ENSO come into play in the Eocene, arguably with more vigor than at any time since then. If a permanent El Niño did occur during the pre–Ice Age Pliocene (*14*), then it should a fortiori have occurred in the Eocene. Currently available Eocene proxy data are insufficient to directly test the permanent El Niño hypothesis: Sparse spatiotemporal coverage renders SST gradients poorly known (*28*), and serious questions have been raised about the accuracy of the estimates themselves (*29*, *30*). Annually resolved paleoclimate proxies from the tropical Pacific, which could provide direct evidence for ENSO, have not been gathered for the Eocene. Several annually resolved middle Eocene records are available, however, in varved sediments from midlatitude lakes. There is a considerable literature on the use of midlatitude proxy data to study past ENSO variability (*31, 32*). The use of such proxy data is possible by virtue of the strong influence ENSO exerts on "teleconnected" midlatitude regions. Studying the deep past with this method, however, requires separate evidence that such teleconnections actually existed during the time period in question. Our strategy is to use a well-tested model to simulate the Eocene climate and determine whether the model predicts significant ENSO variability, with strong teleconnections to those extratropical regions where Eocene varved lakes are found. The model-predicted variability can then be directly compared with that revealed by the sediment records.

We use the Community Climate System Model (CCSM) of the National Center for Atmospheric Research (NCAR) (*25*). The CCSM is a fully coupled, non–flux-corrected ocean–atmosphere–land–sea ice general-circulation model known to produce a faithful reproduction of modern-day ENSO variability (*25*, *33*) and its attendant extratropical teleconnections (*34*) (fig. S1). A recent study (*35*) showed that changing orbital parameters to mid-Holocene values produces a reduction of ENSO amplitude consistent with that found in data (*19*); thus, the model does not produce vigorous ENSO under all circumstances. We integrate the model to equilibrium using a realistic reconstruction of Eocene topography, bathymetry, and vegetation (*36*). In accordance with estimates for the middle Eocene (*21*), the partial pressure of CO_2 (pCO_2) is set at 560 parts per million, about twice the modern, preindustrial value. (Further details on model setup and parameter sensitivity, including to higher pCO_2, are available as Supporting Online Material.)

The equilibrated climate of the Eocene simulation shows Pacific extratropical and deep-ocean temperatures 6° to 13°C warmer than modern values (Fig. 1), in agreement with proxy reconstructions (*15*). Tropical temperatures are only up to 3°C warmer than modern temperatures, with eastern equatorial Pacific SST up to 1°C colder than modern values. The model thus reproduces the general pattern of weakened meridional temperature gradients expected of equable climates such as the Eocene. The presence of wide-open Panamanian and Indonesian seaways weakly impacts ITCZ (Intertropical Convergence Zone) location, eastern equatorial upwelling, and thermocline depth. The east-west SST difference across the equatorial Pacific is ~7°C, slightly higher than modern values, but because the basin is wider, the mean gradient is almost unchanged. Walker-cell strength (as measured by mean surface stress) and thermocline tilt are similar to today's values. An Eocene analog of "13°C" mode water forms just below the equatorial thermocline, with a temperature only ~2°C warmer than modern values despite the much greater warming of >8°C at depth.

Given the similarity of the simulated Eocene tropical mean state to that of today, theory predicts that ENSO should not be fundamentally different from that of today (*37*). The signature of ENSO—basin-scale equatorial SST anomalies coherent with thermocline depth anomalies—is in fact apparent in the Eocene simulation (fig. S4). Equatorial SST variability peaks between 150°E and 160°W; using this region (*38*), we define an "Eocene Niño Index" (ENI) (Fig. 2). Spectral analysis of the ENI time series (Fig. 2) shows a strong interannual band with peaks at 3.3,

Danish Center for Earth System Science, Niels Bohr Institute for Astronomy, Physics, and Geophysics, University of Copenhagen, Juliane Maries Vej 30, DK-2100, Copenhagen Ø, Denmark.

*Present address: Earth and Atmospheric Sciences Department, 1397 Engineering Building, West Lafayette, IN 47907, USA.

†To whom correspondence should be addressed. E-mail: huberm@purdue.edu

4.7, and 5.1 years, together with a distinct quasi-biennial peak at ~2.3 years. The general structure of the spectrum and the specific frequencies are essentially identical to those observed today (*39*, *40*). The magnitude of ENSO is greater than current values; the standard deviation of ENI is 1.13°C (~60% greater than in modern simulations). Regression of surface temperatures onto ENI (Fig. 3) displays the "horseshoe" structure over the Pacific basin familiar from today's climate (fig. S1) (*1*, *2*). The modern dipole over North America is replaced by a single maximum, and teleconnections to proto-Europe are stronger than they are today; such differences are reasonable, considering the changes in continental disposition, orography, vegetation, and GHG forcing. The model's skill in reproducing modern teleconnection patterns (fig. S1) lends credibility to the patterns' Eocene counterparts. Empirical orthogonal function analysis (fig. S2) shows a leading mode similar to the regression pattern in Fig. 3, with a principal component strongly correlated with ENI. Thus, ENSO is the leading source of global interannual variability in the simulation.

We compare model results against middle Eocene lake-sediment records (*41*) from two regions. The best characterized of these records is the Lake Gosiute complex in present-day Wyoming. Spectral analysis of varve thickness has revealed a strong band in the ENSO range, with split peaks at 4.8 and 5.6 years, as well as power at lower, decadal frequencies (*42*). The model (Fig. 3 and fig. S1) independently confirms the speculation in (*42*) that the cause was ENSO. In the Eocene, Lake Gosiute was ~5° to the north and considerably to the east of its current location, in a region we refer to as "proto-Wyoming." Spectral analysis of modeled proto-Wyoming surface temperatures reveals statistically significant bands at 2.25 years and 4.6 to 8 years (Fig. 4). The ENI peaks at 5.5 and 2.4 years (Fig. 2) are coherent with those in the proto-Wyoming spectrum with 99% significance, as is a peak at ~10 years. These results are confirmed by other nearby lake varve records showing nearly identical periodicities (*42*).

Another middle Eocene varved lake, Eckfield Maar in modern Germany, contains evidence of climate variability at 5.5 years, identified here as an ENSO signal, and at 8.7 years (*43*). Today, ENSO impact on Europe is relatively weak, but statistically significant, especially for precipitation and stream flow (*44*, *45*). For the Eocene, the model predicts a fairly strong ENSO teleconnection to proto-Europe in both temperature and precipitation (Fig. 3), which is plausible given the much greater proximity of Europe to America and the Pacific in that period, when the Atlantic was half its present width. Analysis of modeled surface temperature in proto-Germany shows a band of variability between 5 and 7 years, which is coherent with the ENI at the 99% significance level. Precipitation variability is more revealing in this region, with a significant peak at ~5 years and coherence

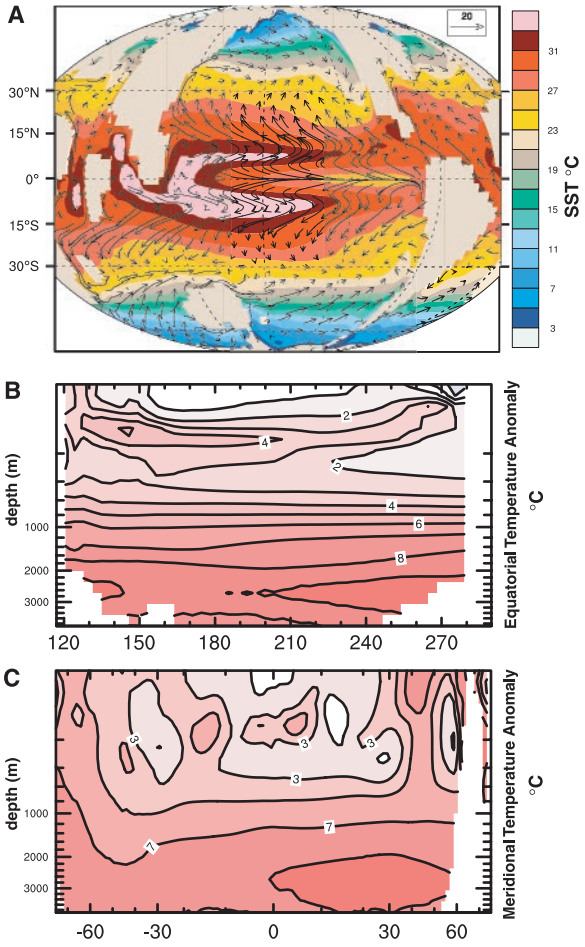

Fig. 1. Annual-mean climatology computed over the last 240 years of the equilibrated Eocene simulation. (**A**) Temperature (contours, 2°C spacing) and currents (arrows; upper right-hand corner shows 20 cm s^{-1} for reference) in the uppermost ocean level (6 m depth). Model resolution is greater than suggested by the density of current vectors, which have been thinned for clarity. (**B**) Eocene-minus-modern ocean temperature difference along the equator. Modern values are taken from an equilibrated run of the same model calculated with modern boundary conditions and preindustrial pCO_2. Horizontal scale shows longitude east of Greenwich. Note the stretched vertical scale. Contour interval is 1°C. (**C**) As in (B) but in the meridional plane, with temperatures averaged between 180° and 130°W. Note the stretched vertical and horizontal scales. Contour interval is 2°C. The full fields are shown in fig. S5.

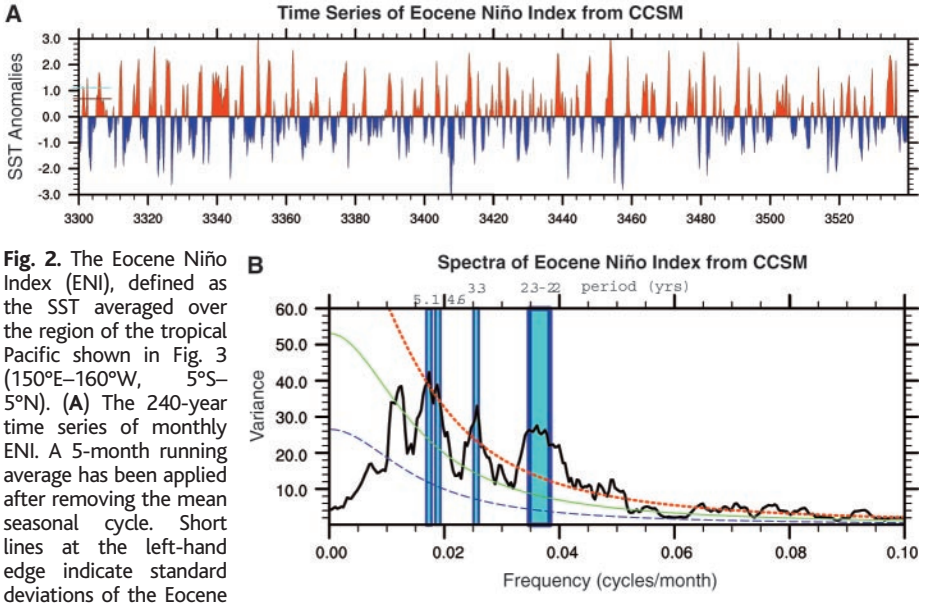

Fig. 2. The Eocene Niño Index (ENI), defined as the SST averaged over the region of the tropical Pacific shown in Fig. 3 (150°E–160°W, 5°S–5°N). (**A**) The 240-year time series of monthly ENI. A 5-month running average has been applied after removing the mean seasonal cycle. Short lines at the left-hand edge indicate standard deviations of the Eocene (blue) and modern (brown) ENSO indices. (**B**) Power spectrum of the ENI (black line). Overlain (green) is the best-fit red noise spectrum and a 95% confidence envelope (dashed lines). Blue bands highlight salient spectral features (with periods noted along the top). The seasonal cycle was removed but no prereddening was performed before computing the spectrum.

with ENI at 5 and 8 years, also significant at the 99% level (Fig. 4).

Thus, the model predicts Eocene ENSO variability similar in frequency and spatial structure and somewhat greater in amplitude than it is today, and this prediction is confirmed by evidence of ENSO–time-scale variability in middle Eocene varved sediments from lakes lying in two teleconnected regions. The model-data agreement provides strong evidence against the hypothesis that "hothouse" climates tend to collapse onto a permanent El Niño state. Our results indicate that the tropical upper-ocean structure in warm climates is close to the modern one, featuring a strong mean east-west SST gradient. We suggest that about half of the spread between recent, controversially warm Eocene SST estimates for the tropical Western Indo-Pacific (*29*) and the much cooler values previously estimated for the central equatorial Pacific (*16*) may be explained by just such a substantial temperature gradient. At the same time, the deep ocean can become much warmer than it is today (~10°C simulated here), in agreement with proxy reconstructions of deep-ocean temperature (*15*). This decoupling of the upper from the deep ocean is consistent with theories for multiple, dynamically independent thermoclines (*46*) and, if true, is a vital clue to understanding how the ocean responds to global warming. Future results arising from the Ocean Drilling Program, especially from the recent Legs 198 and 199 in the Pacific, may further constrain the mean tropical climate state; we suggest that the collection of annually resolved Eocene records from the tropical Pacific (e.g., corals) or teleconnected midlatitude regions (e.g., tree rings, varves) may also provide further crucial insights into the stability of the tropical mean state and its variability.

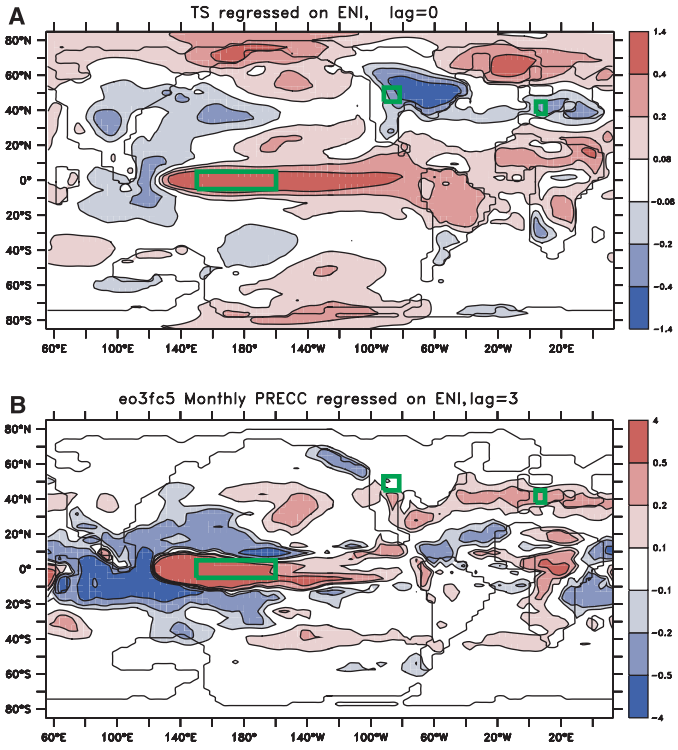

Fig. 3. Monthly mean Eocene model surface temperature (°C) in (**A**) and total precipitation in (**B**), regressed onto the ENI. The seasonal cycle was removed from the 240 years of data used in the computation. The large green box in the equatorial Pacific shows the region used to define the ENI. The two smaller green boxes indicate the regions in proto-Wyoming and proto-Germany containing the varved Eocene lakes discussed in the text. (Further analysis may be found in the Supporting Online Material.)

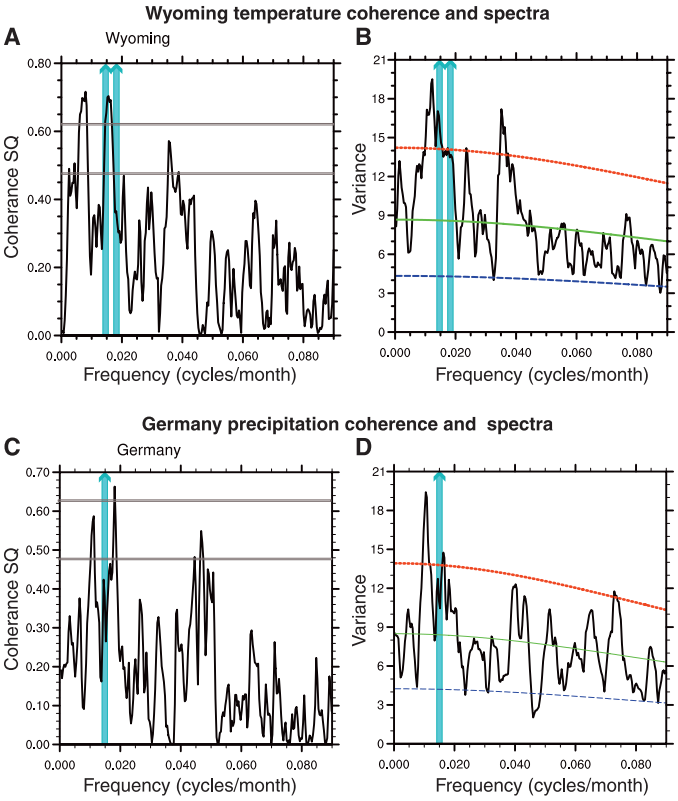

Fig. 4. (**A**) Spectral coherence between modeled surface temperature in proto-Wyoming and ENI. Horizontal lines indicate 95 and 99% significance levels. (**B**) Power spectrum of modeled surface temperature in proto-Wyoming. Overlain (green line) is the best-fit red noise spectrum and a 95% confidence envelope (dashed lines). (**C**) and (**D**) show the same analysis, but for precipitation in proto-Germany. The monthly temperature and precipitation values were averaged over the boxes shown in Fig. 3, and the seasonal cycle was removed before analysis. Blue arrows indicate the dominant peaks revealed by proxy data studies in those locations (*42*, *43*).

References and Notes

1. K. E. Trenberth, J. M. Caron, D. P. Stepaniak, S. Worely, *J. Geophys. Res.* **107** 10.1029/2000JD000298 (2002).
2. H. F. Diaz, M. P. Hoerling, J. K. Enscheid, *Int. J. Climatol.* **21**, 1845 (2001).
3. R. A. Feely, R. Wanninkhof, T. Takahashi, P. Tans, *Nature* **398**, 597 (1999).
4. M. A. Cane, *Science* **282**, 59 (1998).
5. J. Cole, *Science* **291**, 1496 (2001).
6. H. A. Dijkstra, J. D. Neelin, *J. Clim.* **8**, 1343 (1995).
7. F. F. Jin, *Science* **274**, 76 (1996).
8. Z. Y. Liu, B. Huang, *J. Clim.* **10**, 1662 (1997).
9. R. T. Pierrehumbert, *Proc. Natl. Acad. Sci. U.S.A.* **97**, 1355 (2000).
10. In the equatorial Pacific, the prevailing easterly surface winds drive an east-west tilting of the thermocline (the region of sharp vertical temperature gradients separating warmer water in the upper ocean from cooler water below). The tilting causes cool subthermocline water to upwell in the east. The resulting gradient in SST between the Cold Tongue in the east and the Warm Pool in the west drives an east-west overturning circulation in the atmosphere, known as the Walker cell, which enhances surface easterlies and produces further upwelling. This positive feedback, first recognized by Bjerknes (*47*), controls both the time-mean state (*6*–*8*) and the interannual (ENSO) variability (*12*) of the tropical Pacific. By "weakening of the Bjerknes feedback," we mean either a weakening of the atmospheric response to a given SST anomaly or a weakening of the oceanic response to a given surface stress anomaly. We focus mostly on this latter effect, which can be achieved by making the mean thermocline deeper and/or reducing the temperature difference across it (*11*).
11. A. V. Fedorov, S. G. Philander, *Science* **288**, 1997 (2000).
12. J. D. Neelin *et al.*, *J. Geophys. Res.* **103**, 14261 (1998).
13. D. Z. Sun, K. E. Trenberth, *Geophys. Res. Lett.* **25**, 2659 (1998).
14. P. Molnar, M. A. Cane, *Paleoceanography* **17**, 10.1029/2001PA000663 (2002).
15. J. Zachos *et al.*, *Science* **292**, 686 (2001).
16. T. Bralower *et al.*, *Paleoceanography* **10**, 841 (1995).
17. D. Z. Sun, *Geophys. Res. Lett.* **24**, 2031 (1997).
18. D. T. Rodbell *et al.*, *Science* **283**, 516 (1999).

19. A. W. Tudhope *et al.*, *Science* **291**, 1511 (2001).
20. It has been suggested that orbitally driven changes in insolation can modulate ENSO (*48*). We do not pursue this issue here, because our purpose is to understand whether reduced or absent ENSO is an inherent, permanent feature of warm climates. Our results do not exclude the possibility that cyclical modulation of ENSO on Milankovich time scales occurred also during the Eocene.
21. D. L. Royer, R. A. Berner, D. J. Beerling, *Earth Sci. Rev.* **54**, 349 (2001).
22. A. Timmermann *et al.*, *Nature* **398**, 694 (1999).
23. G. A. Meehl *et al.*, *J. Clim.* **13**, 1879 (2000).
24. M. Collins, *J. Clim.* **13**, 1299 (2000).
25. M. Blackmon *et al.*, *Bull. Am. Meteorol. Soc.* **82**, 2357 (2001).
26. W. P. Chaisson, A. C. Ravelo, *Paleoceanography* **15**, 497 (2000).
27. M. A. Cane, P. Molnar, *Nature* **411**, 157 (2001).
28. M. Huber, L. C. Sloan, *Paleoceanography* **15**, 443 (2000).
29. P. N. Pearson *et al.*, *Nature* **413**, 481 (2001).
30. D. P. Schrag, *Chem. Geol.* **161**, 215 (1999).
31. T. M. Rittenour, J. Brigham-Grette, M. E. Mann, *Science* **288**, 1039 (2000).
32. M. E. Mann, R. S. Bradley, M. K. Hughes, in *El Niño and the Southern Oscillation: Multiscale Variability and Global and Regional Impacts,* H. F. Diaz, V. Markgraf, Eds. (Cambridge Univ. Press, Cambridge, 2000), pp. 357–412.
33. B. L. Otto-Bliesner, E. C. Brady, *J. Clim.* **14**, 3587 (2001).
34. I.-S. Kang *et al.*, *J. Clim.* **15**, 2791 (2002).
35. B. L. Otto-Bliesner, E. C. Brady, C. Shields, *Eos* **83**, (Fall Meet. Suppl.), abstract PP72B-03 (2002).
36. M. Huber, L. C. Sloan, *Geophys. Res. Let.* **28**, 3481 (2001).
37. Specifically, we compare values with the theoretical framework of (*11*). Our simulated values of easterly surface wind stress along the equator (~0.5 dyn cm^{-2}) and mean thermocline depth (~120 m) (fig. S5) place the Eocene simulation near the point marked "A" in their figure 4a, i.e., near modern values. The ENSO period associated with these conditions is ~5 years, matching those found in Eocene simulations and proxy records.
38. Today, maximum SST variability is found farther east, in the "Niño 3" (150°W to 90°W) and "Niño 3.4" (170°W to 120°W) regions. Given the different basin geometry in the Eocene simulation, a shift in location is not surprising. Today, the Niño 3.4 region brackets the zone where the Cold Tongue impinges on the Warm Pool. Thus, it strongly affects precipitation and hence diabatic heating and atmospheric circulation, making it the preferred region for studies of extratropical ENSO impacts. Precisely the same role is played in the Eocene simulation by our "Eocene Niño" region.
39. R. J. Allan, in *El Niño and the Southern Oscillation: Multiscale Variability and Global and Regional Impacts,* H. F. Diaz, V. Markgraf, Eds. (Cambridge Univ. Press, Cambridge, 2000), pp. 3–55.
40. M. Ghil *et al.*, *Rev. Geophys.*, 10.1029/2000RG000092, 13 September 2002.
41. Lake sediments are affected by a number of seasonally varying factors, including temperature, insolation, snowmelt, runoff, and surface wind speed (*49*), whose interannual variations are recorded by changing layer thickness. Here, we concentrate on surface temperature and precipitation results.
42. M. Ripepe, L. T. Roberts, A. G. Fischer, *J. Sediment. Petrol.* **61**, 1155 (1991).
43. J. Mingram, *Palaeogeogr. Palaeoclimatol. Palaeoecol.* **140**, 289 (1998).
44. K. Fraedrich, *Tellus* **46A**, 541 (1994).
45. G. J. van Oldenborgh, G. Burgers, A. K. Tank, *Int. J. Climatol.* **20**, 565 (2000).
46. G. K. Vallis, *J. Phys. Oceanogr.* **30**, 933 (2000).
47. J. Bjerknes, *Mon. Weather Rev.* **97**, 163 (1969).
48. A. C. Clement, R. Seager M. A. Cane, *Paleoceanography* **15,** 731 (2000).
49. C. Morrill, E. E. Small, L. C. Sloan, *Global Planet. Change* **29**, 57 (2001).
50. M. H. acknowledges L. C. Sloan for mentorship and support by NSF ATM9810799 and the Packard Foundation. This study would not have been conducted without B. Otto-Bliesner and E. Brady having first demonstrated ENSO in their Cretaceous simulation. We authors also thank F. F. Jin, Z. Y. Liu, M. A. Cane, and S. G. Philander for sharing their ideas. The CCSM model, computer time, and graphics tools (NCAR Command Language, NCL) were provided through NCAR by the NSF. Support for both authors was provided by Dansk Grundforskningsfond through the Danish Center for Earth System Science.

Supporting Online Material
www.sciencemag.org/cgi/content/full/299/5608/877/DC1
Materials and Methods
Figs. S1 to S6
References

25 September 2002; accepted 2 January 2003

Lipid-Like Material as the Source of the Uncharacterized Organic Carbon in the Ocean?

Jeomshik Hwang and Ellen R. M. Druffel

The composition and formation mechanisms of the uncharacterized fraction of oceanic particulate organic carbon (POC) are not well understood. We isolated biologically important compound classes and the acid-insoluble fraction, a proxy of the uncharacterized fraction, from sinking POC in the deep Northeast Pacific and measured carbon isotope ratios to constrain the source(s) of the uncharacterized fraction. Stable carbon and radiocarbon isotope signatures of the acid-insoluble fraction were similar to those of the lipid fraction, implying that the acid-insoluble fraction might be composed of selectively accumulated lipid-like macromolecules.

Less than 40% of sinking POC collected below the euphotic zone can be molecularly characterized (*1*, *2*). The uncharacterized fraction constitutes an increasing proportion of POC with the depth at which it is collected, with the highest fraction in sedimentary organic carbon (*1*). What is the composition of the uncharacterized fraction and how is it formed?

One hypothesis for the formation of the uncharacterized fraction is abiological recombination of small molecules such as amino acids and carbohydrates produced by degradation of labile organic matter (*3*, *4*). This hypothesis has been challenged by results of ^{13}C and ^{15}N nuclear magnetic resonance (NMR) spectroscopy (*5*, *6*). A second hypothesis is that biologically produced refractory compounds are selectively accumulated whereas labile compounds are remineralized (*7*, *8*). Hydrolysis-resistant cell wall–derived material has been observed in recent and ancient sediments (*9*–*11*). A third hypothesis involves physical protection of organic carbon by refractory organic or inorganic matrices (*12*, *13*). A recent study explored solid-state ^{13}C NMR spectra of plankton and sinking POC collected at shallow and deep waters (*14*). The similarity of the spectra led Hedges *et al*. to suggest that the uncharacterized fraction was the same organic material produced biologically but was protected by mineral matrices or refractory biomacromolecules.

Department of Earth System Science, University of California Irvine, Irvine, CA 92697–3100, USA. E-mail: jeomshik@uci.edu (J.H.); edruffel@uci.edu (E.R.M.D.)

Biologically produced lipids, amino acids, and carbohydrates have distinct stable carbon isotope [$\delta^{13}C$ (*15*)] signatures because of the different physiological fractionation of carbon during their syntheses (*16*, *17*). Therefore, comparison of the $\delta^{13}C$ signature of the uncharacterized fraction with those of other organic fractions will provide insights as to its source(s). The radiocarbon isotope [$\Delta^{14}C$ (*18*)] signatures of all organic fractions are the same when measured in plankton from the surface water because they are fractionation-corrected. The overall signature changes when carbon with a different $\Delta^{14}C$ signature is incorporated and when the carbon is aged (*19*). Therefore, organic fractions that have similar sources, sinks, and residence times in the ocean will have similar $\Delta^{14}C$ signatures.

We measured $\delta^{13}C$ and $\Delta^{14}C$ values in sinking POC collected from a depth of 3450 m, at a site (Station M, 4100 m deep at the bottom, 34°50′N, 123°00′W) 220 km west of the California coast. We isolated biologically important compound classes: lipids, total hydrolyzable amino acids (THAA), total hydrolyzable neutral carbohydrates (TCHO), and a proxy of the uncharacterized fraction, the acid-insoluble fraction (*20*). The acid-insoluble fraction that remains after organic solvent extraction and acid hydrolysis accounts for ~70% of the uncharacterized fraction (*21*).

Sinking POC originates mainly from dissolved inorganic carbon (DIC) in surface waters, and it reaches the deep water on a time scale of months. Therefore, bulk sinking POC